A CFD-DEM approach to study the breakup of fractal agglomerates in an internal mixer

Received: 25 November 2019 | Revised: 7 February 2020 | Accepted: 26 February 2020

DOI: 10.1002/cjce.23773

SPECIAL ISSUE ARTICLE

THE CANADIAN JOURNAL OF CHEMICAL ENGINEERING

Canadian Society for Chemical Engineering | For Our Future
Société canadienne de génie chimique | Pour notre avenir

A CFD-DEM approach to study the breakup of fractal agglomerates in an internal mixer

Graziano Frungieri[1] | **Gianluca Boccardo**[1] | **Antonio Buffo**[1] | **Daniele Marchisio**[1] | **Hossein Ali Karimi-Varzaneh**[2] | **Marco Vanni**[1]

[1]Department of Applied Science and Technology, Politecnico di Torino, Torino, Italy

[2]Continental Reifen Deutschland GmbH, Hannover, Germany

Correspondence
Graziano Frungieri, Department of Applied Science and Technology, Politecnico di Torino, Corso Duca degli Abruzzi 24, 10129 Torino, Italy.
Email: graziano.frungieri@polito.it

Funding information
H2020 project VIMMP: VIRTUAL MATERIAL MARKETPLACE, Grant/Award Number: 760907

Abstract

In this work we present a method to investigate the breakup of filler agglomerates in an internal mixer during a compounding operation. The method employs computational fluid dynamics (CFD) simulations along with discrete element method (DEM) simulations. CFD simulations are performed to compute the flow field inside a 2D section of a typical batch internal mixer with two tangential rotors. During the CFD simulation, we assume the filler agglomerates to behave as tracer particles, carried passively by the flow. The trajectory of the tracers, together with the experienced velocity gradients, are fed to a DEM code, built in the framework of Stokesian dynamics. The code computes the mechanical response of the agglomerates along the trajectory, from which it is finally possible to ascertain the occurrence of breakup. Simulations are performed to evaluate the robustness of the method on two different rotor speed ratio conditions and varying agglomerate strength.

KEYWORDS

agglomerate breakup, dispersive mixing, internal mixer, polymer compounds, Stokesian dynamics

1 | INTRODUCTION

Many solid filler particles used in rubber and plastic compounds exist in the form of agglomerates of primary particles kept together by the action of surface forces. During the compounding operation, such agglomerates are broken down into smaller fragments and uniformly redistributed throughout the medium.[1] The compounding operation is generally carried out in an internal mixer, a sophisticated heavy equipment, consisting of a pair of complex-shaped rotors with a variable number of wings, counter-rotating in an enclosed chamber. The chamber is formed by two lobes designed in such a way as to accommodate the rotors, leaving a small gap between the tips of the wings and the chamber wall.[2,3]

Several studies have investigated the flow dynamics in such a mixing equipment for different rotor designs and operative conditions, such as rotor speed ratio, fill factor, and batch temperature, by using flow visualization techniques,[4–6] or computational fluid dynamics simulation.[7–13] However, the studies of the effect of the flow field on the filler breakup has been so far limited to a generic analysis of the flow characteristics,

in terms of shear rate and mixing index, or were based on simplified approaches for the agglomerate breakup mechanism.[14]

It is well known that the breakup of agglomerates occurs when the internal stresses, induced by the viscous forces due to the flow, exceed a certain threshold value. Based on this argument, a number of modelling approaches have been proposed over the years to predict the breakup of agglomerates. The first studies adopted idealized representations of the agglomerates as spherical objects with uniform,[15] radially varying porosity,[16] or as pairs of contacting particles.[17] However, these simplified views are not able to take into account the presence of weak points and local heterogeneities in the agglomerate structure, which may play an important role in the breakup mechanism.[18] This has led to the use of discrete element methods (DEM), which are able to take into full account the peculiar disordered structure of the agglomerates, including the role that each primary particle plays in the transmission of stresses.[19]

Different degrees of complexity can be introduced in DEM simulations of agglomerate breakup. Most approaches adopted the free-draining approximation, where each monomer is assumed to experience the Stokes drag force, as if no other particle were in the flow.[20] However, the hydrodynamic screening effects taking place in the agglomerate were seen to play a non-negligible role.[21,22] This effect can be taken into account by modelling the hydrodynamic screening by geometrical considerations,[23,24] or by the method of reflections.[25] However, more accurate predictions are given by Stokesian dynamics.[26,27] This method, by using a first-order expansion of the exact solution of the flow field, is able to evaluate the hydrodynamic forces acting on each monomer for any possible spatial arrangement.[28,29] Stokesian dynamics simulations have been performed over the years to predict momomer aggregation,[30] agglomerate restructuring,[31] and the breakup of soft and rigid agglomerates in both simple flow configurations[32–34] and in turbulent conditions.[35]

In this work we make use of Stokesian dynamics, coupled with CFD simulations, to study the breakup of fractal agglomerates in the complex flow field of an internal mixer. The flow field inside the mixing equipment is computed by transient CFD simulation performed by the CFD code Ansys Fluent 19.2; during the CFD simulations, the agglomerates are treated as passive tracer particles, whose trajectories are recorded together with the viscous stress experienced during the motion. This piece of information is then used by a discrete element method, built in the framework of Stokesian dynamics. At this stage the disordered structure of the agglomerates is modelled in detail and the DEM returns the hydrodynamic forces acting on each constituent monomer as well as the mechanical stresses acting on each single inter-monomer contact. Since we deal here with statically determined agglomerate structures, this information can be used to evaluate the occurrence of breakup. To our knowledge, this is the first attempt to address jointly the role that the flow field and the agglomerate structure plays in a compounding operation.

The effort of coupling CFD with Stokesian dynamics is carried out in the context of the H2020 VIMMP project, which aims to develop an open, interoperable, and ontology-based simulation platform for multi-scale modelling.[36]

2 | NUMERICAL METHOD

2.1 | Main assumptions

We assume the dispersing medium to be a highly viscous Newtonian medium and the filler particles to consist of neutrally buoyant micron-sized agglomerates. We further assume that the medium completely wets the surface of each monomer composing the agglomerates. The main parameters of the simulations are reported in Table 1. Given their small size and the large viscosity of the medium, the particle Reynolds number and the particle Stokes number are much lower than the unity for such a case, meaning that the response of the agglomerates to changes in the flow field is fast and that the inertia of the agglomerates is negligible. Therefore, their motion can be reduced to that of tracer particles and their equation of motion is the advection equation:

$$\dot{\boldsymbol{x}}_p(t) = \boldsymbol{u}\left(\boldsymbol{x}_p(t), t\right) \tag{1}$$

where $\mathbf{u}(\mathbf{x}_p(t), t)$ is the velocity of the flow at the tracer particle position.

Given their small size, we can safely further assume that the agglomerates experience locally along their

TABLE 1 Main parameters of the CFD-DEM simulation

Parameter	Symbol	Value
Medium viscosity	μ	4.5×10^4 Pa · s
Medium density	ρ_f	1000 kg · m^{-3}
Agglomerate gyration radius	R_g	0.74-3.46 μm
Monomer radius	a	100 nm
Rotor velocity	$\dot{\theta}$	2.512-3.768 rad · s^{-1}
Rotor tip radius	d_{tip}	0.743 m
Number of tracer particles	N_t	1000

trajectory a linear flow field, which can be fully described by the local components of the velocity gradients. Under these circumstances, Stokesian dynamics can be adopted to evaluate the phenomena occurring at the agglomerate scale. By using the information on the velocity gradients at the location of the agglomerates and by taking into account their actual morphology, Stokesian dynamics predicts both the rotational component of the motion of the agglomerates and the hydrodynamic forces acting on all the constituent monomers. From this information, it is possible to evaluate the internal forces acting at the inter-monomer contacts. As the agglomerates studied in this work are rigid and isostatic, the failure of a single inter-monomer bond leads to the breakup of the agglomerate and we assume that breakup occurs instantaneously as soon as the tensile force on the most loaded bond exceeds a critical threshold tensile stress.

2.2 | CFD simulations

Since the study of dispersive mixing is the main focus of this work, the motion of the material along the axial direction of the internal mixer was here disregarded and 2D simulations of the mixer were performed. The flow field was evaluated by isothermal unsteady simulations run by using Ansys Fluent 19.2. The field equations in this case read as follows:

$$\frac{\partial u_i}{\partial x_i} = 0 \tag{2}$$

$$\rho\frac{\partial u_i}{\partial t} + \rho\frac{\partial \left[u_i u_j\right]}{\partial x_j} = -\frac{\partial p}{\partial x_i} + \frac{\partial \sigma_{ij}}{\partial x_j} \tag{3}$$

where the u_i's are the velocity components of the flow; and $\sigma_{ij} = \mu(du_i/dx_j + du_j/dx_i) = 2\mu E_{ij}$ is the viscous stress tensor. In Equation (3), one can notice that, because of the lack of inertia of the suspended particles, no terms accounting for the back reaction of the particle on the flow are included.

The medium is mechanically stirred by the motion of two counter-rotating tangential rotors in a completely filled chamber. To handle the variation in time of the shape of the flow domain, a sliding mesh approach was adopted; the flow domain was therefore split in three distinct cell regions: two rotor regions and one stator region, as illustrated in Figure 1. The first ones rotate together with the rotors, while the second remains fixed. Thus, the grids slide past each other along two circular interfaces. No slip boundary conditions were imposed at the rotor and stator walls. The mesh is composed of 45 920 quadrilateral cells. The region between the rotor tip and the chamber wall, which is the region where high shear forces are established, is resolved using seven layers; this resolution was able to capture all the features of the flow field.

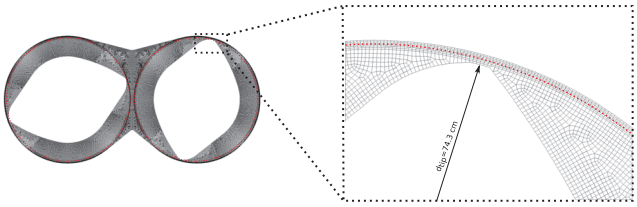

FIGURE 1 Mesh used for the investigation. The mesh is composed of 45 920 cells. The sliding interfaces separating the three cell zones are depicted in red

Two different speed ratios of the rotors were investigated, 1:1 (30 rpm:30 rpm) and 1:1.5 (24 rpm:36 rpm). Starting from the relative configuration of the rotors of Figure 1, two complete periods were simulated with a time step $\Delta t = 10^{-3}$ seconds. In the case of rotors both rotating at 30 rpm, this leads to a simulated time equal to 4 seconds and to an angle spanned by the rotors per time step equal to 0.05°.

At each time step, the six field quantities corresponding to velocity (u_i) and velocity gradients (du_i/dx_j) evaluated at the centre of each interior face and at the centre of each boundary edge were stored. These quantities were used to extract the trajectories of a set of tracer particles and the velocity gradients they experience along their trajectory. For this purpose, the modified Shepard algorithm was used.[37] The algorithm computes a quadratic, smooth, once continuously differentiable bivariate function, which interpolates the field data at the scattered nodes (x,y) and can be then evaluated at arbitrary points within the domain. Given the transient nature of the flow, the interpolants had to be recomputed on each instantaneous field data and the calculation scheme was therefore as follows:

1 The initial position of the particle is chosen.
2 The interpolants of the six field quantities are computed on the instantaneous field data.
3 The six quantities (u_i and du_i/dx_j) at the particle positions $\mathbf{x}_p$ are evaluated.
4 The velocity components u_i are used to obtain the new particle position by an explicit Euler integration of Equation (1).
5 The field data is updated for the new time step.
6 Back to point 2.

It is worth pointing out that the same time resolution was used for the solution of the flow dynamics and the

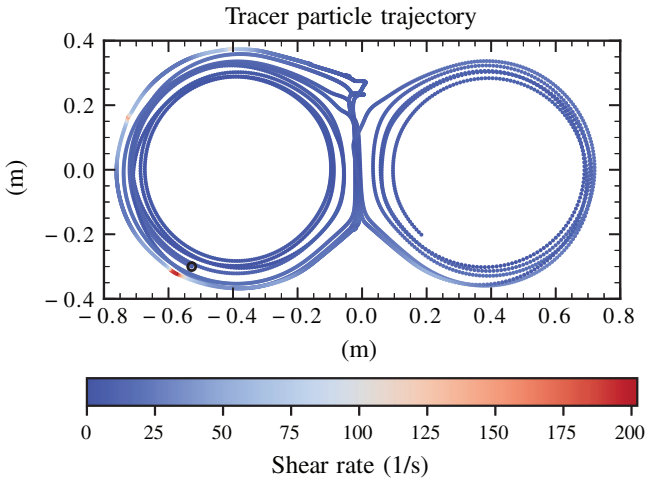

FIGURE 2 Trajectory of a sample tracer particle. The shade intensity represents the shear rate experienced by the particle. The starting point of the particle trajectory is highlighted by a small circle

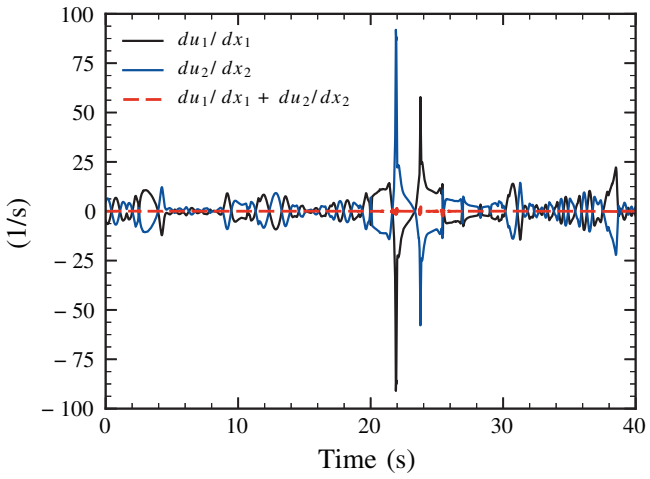

FIGURE 3 Velocity gradients components along a trajectory. Please note that, because of the periodic nature of the flow, trajectories could be extended over the time lapse simulated by the computational fluid dynamics simulations

particle trajectories. In Figure 2, the trajectory of a sample tracer particle is shown. In Figure 3, two components of the velocity gradient tensor independently evaluated at the particle position are plotted against the temporal coordinate. From the plot it is possible to discern that the continuity condition is respected remarkably well at any point of the particle trajectory, proving the adequate efficacy of the interpolation scheme on the adopted grid resolution.

2.3 | DEM simulations

In the discrete element method simulations, the morphology of the agglomerates is fully taken into account. A library of agglomerates was generated numerically by using a tunable cluster-cluster method, able to produce agglomerates with a prescribed fractal dimension d_f,[38,39] which was set to $d_f = 1.8$ for the agglomerates used in our simulation. The generation started from a population of trimers and proceeded hierarchically through the collision of equal sized clusters with the generation of one single new contact at each aggregation event and no restructuring effects were taken into account. As a consequence, the agglomerates have an isostatic structure and the failure of any of the their bonds leads to the fragmentation in two smaller fragments. Unless stated otherwise, the results herein reported refer to the agglomerate population whose main properties are reported in Table 2. In order to extract reliable statistics, for each class we studied 100 different agglomerates realizations.

DEM simulations were run to investigate the mechanical response of the agglomerates to the stress

TABLE 2 Properties of the investigated agglomerates

n_m	48	96	192	384	768
R_g/a	7.425	10.913	16.040	23.574	34.648

Note: For each family of agglomerates $n_m = k_f (R_g/a)^{d_f}$, with $k_f = 1.3$ and $d_f = 1.8$. The monomer radius is $a = 100$ nm.

exerted by the flow field. As previously pointed out, the size of the agglomerates is small compared to the typical distances over which the variation of the velocity gradients takes place. Therefore, it is reasonable to assume that the agglomerates are surrounded by a linear flow field with uniform velocity gradients, whose history is provided by the CFD simulations.

As a consequence, in a reference frame moving with the agglomerate, the undisturbed velocity at the position occupied by any monomer composing the cluster can be computed as $\mathbf{u}_m^\infty(\mathbf{x}) = \nabla\mathbf{u}^\infty \cdot \mathbf{x}_m$, where $\nabla\mathbf{u}^\infty$ is the velocity gradient tensor evaluated at the position of the centre of mass of the agglomerate and $\mathbf{x}_m$ is the position vector of the m-th monomer with respect to the centre of mass of the agglomerate. Please note that in the following the superscript ∞ is used to distinguish between the undisturbed flow velocity and the monomer velocities.

Under the condition of a vanishingly small particle Reynolds number, it is possible to evaluate the hydrodynamic forces and torques acting on each monomer of the agglomerate resorting to Stokesian dynamics. This method, employed here in its most accurate formulation (force-torque-stresslet), provides the relation between the hydrodynamic force and the relative velocity of the

monomers compared to the velocity of the undisturbed flow at the monomer position. The relation between such quantities is of the following kind:

$$\frac{1}{\mu}\begin{bmatrix} M^{UF} & M^{UT} & M^{US} \\ M^{\Omega F} & M^{\Omega T} & M^{\Omega S} \\ M^{EF} & M^{ET} & M^{ES} \end{bmatrix} \begin{Bmatrix} \mathbf{F} \\ \mathbf{T} \\ \mathbf{S} \end{Bmatrix} = - \begin{Bmatrix} \mathbf{u} - \mathbf{u}^{\infty}(\mathbf{x}) \\ \boldsymbol{\omega} - \boldsymbol{\omega}^{\infty} \\ -\mathbf{E}^{\infty} \end{Bmatrix} \tag{4}$$

where $\mathbf{u} = (\mathbf{u}_1, ..., \mathbf{u}_m, ..., \mathbf{u}_{n_m})$ and $\boldsymbol{\omega} = (\boldsymbol{\omega}_1, ..., \boldsymbol{\omega}_m, ..., \boldsymbol{\omega}_{n_m})$ are the vectors of the linear and angular velocities of the monomers composing the agglomerate, $\boldsymbol{\omega}^{\infty}$ is the angular velocity of the undisturbed flow field and $\mathbf{u}^{\infty}(\mathbf{x})$ is the linear velocity of the undisturbed flow at the monomer position. $\mathbf{F} = (\mathbf{f}_1, ..., \mathbf{f}_m, ..., \mathbf{f}_{n_m})$ and $\mathbf{T} = (\mathbf{t}_1, ...\mathbf{t}_m, ..., \mathbf{t}_{n_m})$ are respectively the hydrodynamic force and torque acting on the monomers. Force, torques, and velocity are three-component vectors, whereas the rate-of-strain tensor and the stresslet tensors, that are symmetric and traceless, are conveniently reduced to the equivalent five-component column vectors $\boldsymbol{E}^{\infty} = (\boldsymbol{e}_1, ..., \boldsymbol{e}_m, ..., \boldsymbol{e}_{n_m})$, where for each monomer $\mathbf{e}_m = \left(e^{\infty}_{xx} - e^{\infty}_{zz}, 2e^{\infty}_{xy}, 2e^{\infty}_{xz}, 2e^{\infty}_{yz}, e^{\infty}_{yy} - e^{\infty}_{zz}\right)$, and $\mathbf{S} = (\mathbf{s}_1, ...\mathbf{s}_m, ..., \mathbf{s}_{n_m})$, where $\mathbf{s}_m = (s_{m,\,xx}, s_{m,\,xy}, s_{m,\,xz}, s_{m,\,yz}, s_{m,\,yy})$. The coefficient matrix, generally referred to as mobility matrix, is used here in its far-field formulation.[26] In the original version of Stokesian dynamics, the far field matrix was corrected for near-field effects to account for the lubrication interaction between particles in relative motion. In our case, however, the correction is neglected because agglomerates are rigid and all the constituent monomers move at the same velocity (Figure 4A). Under the condition of rigid body motion it is possible to write the following:

$$\begin{cases} \mathbf{u}_m = \mathbf{u}_{cm} + \boldsymbol{\omega}_{cm} \times (\mathbf{x}_m - \mathbf{x}_{cm}) \\ \boldsymbol{\omega}_m = \boldsymbol{\omega}_{cm} \end{cases} \quad m = 1, 2, ..., n_m \tag{5}$$

Furthermore, the assumption that the agglomerate has negligible inertia and is carried passively by the fluid implies that no net force or torque acts on it, and hence:

$$\begin{cases} \sum_m \mathbf{f}_m = 0 \\ \sum_m (\mathbf{t}_m + (\mathbf{x}_m - \mathbf{x}_{cm}) \times \mathbf{f}_m) = 0 \end{cases} \quad m = 1, 2, ..., n_m \tag{6}$$

By substituting Equation (5) in Equation (4) and including Equation (6) in the resulting system, one finally obtains the following linear system:

$$\begin{bmatrix} \frac{1}{\mu}M^{UF} & \frac{1}{\mu}M^{UT} & \frac{1}{\mu}M^{US} & A \\ \frac{1}{\mu}M^{\Omega F} & \frac{1}{\mu}M^{\Omega T} & \frac{1}{\mu}M^{\Omega S} & B \\ \frac{1}{\mu}M^{EF} & \frac{1}{\mu}M^{ET} & \frac{1}{\mu}M^{ES} & C \\ A^T & B^T & C^T & D \end{bmatrix} \begin{Bmatrix} \mathbf{F} \\ \mathbf{T} \\ \mathbf{S} \\ \mathbf{u}_{cm} \\ \boldsymbol{\omega}_{cm} \end{Bmatrix} = \begin{Bmatrix} \mathbf{u}^{\infty} \\ \boldsymbol{\omega}^{\infty} \\ \mathbf{E}^{\infty} \\ -\mathbf{0} \\ -\mathbf{0} \end{Bmatrix} \tag{7}$$

whose solution provides the values of the $(11n_m + 6)$ unknowns corresponding to the forces $\mathbf{F}$, the torques $\mathbf{T}$, and the stresslets $\mathbf{S}$ acting on the individual monomers and the translational and angular velocities of the centre of mass of the agglomerate, $\mathbf{u}_{cm}$ and $\boldsymbol{\omega}_{cm}$. The angular velocity of the agglomerate was integrated in time to take into account the orientation dynamics of the agglomerate during its motion. Further details about the method, its implementation and the expression for the coefficient matrix appearing in Equation (7) can be found elsewhere.[26,33,35]

Since the structure of our agglomerates is statically determined, the evaluation of the internal stress is straightforward; from the computed hydrodynamic forces $\mathbf{f}_m$ and torques $\mathbf{t}_m$ acting on each monomer of the agglomerate, the contact forces $\mathbf{F}^c_{mn}$ and torques $\mathbf{T}^c_{mn}$ acting at each contact can be readily obtained by imposing simple force and torque balances for each monomer, as illustrated in Figure 4B,C. The tensile force N at each contact follows immediately from the decomposition of the computed contact forces and, for the isostatic aggregates considered here, it can be shown that $N \propto \mu a^2 \dot{\gamma}$ (see supporting information in Vanni and Gastaldi[32]).

2.4 | Computational effort

All the simulations were run on a workstation equipped with a Intel(R) Xeon(R) CPU E5-2630 v4 @ 2.20GHz.

The CFD simulations were run using four processing cores exploiting the MPI parallel solver of Ansys Fluent 19.2. The simulations required approximately 60 wall-clock minutes per physical-time second.

The interpolation and tracking algorithm was run using seven CPUs exploiting MPI parallelism. Six processes were used to interpolate the six field quantities of

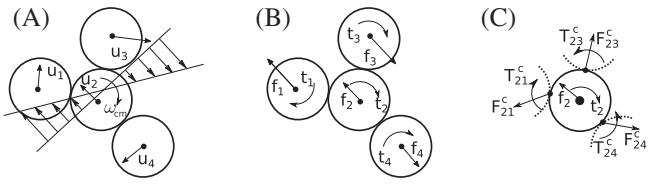

FIGURE 4 A, Sample isostatic agglomerate in planar shear; B, hydrodynamic force and torques acting on the monomers; and C, force-torque balance on a single monomer

interest (two linear velocities and four gradient components) and to perform the evaluation of the field data at the particle position. One additional master process was used to collect the data and to compute trajectories. The execution of the code for the tracking of 1000 tracer particles required 50 wall-clock minutes per physical-time second.

For our DEM simulations, the wall-clock time scales approximately with the square of the number of monomers composing the agglomerate for a fixed number of processing cores. The use of two OpenMP threads for the simulation of an agglomerate composed of 768 monomers required 70 wall-clock seconds per physical-time second.

3 | RESULTS

3.1 | Flow field characterization

The flow field inside the mixing equipment was computed for two different speed ratios. Some instantaneous data fields for the 1:1 speed ratio case are reported in Figure 5A-D. It was seen that in most of the domain, the fluid just undergoes a circular motion, with a maximum circumferential velocity that is consistent with the maximum tangential velocity imposed by the rotor rotation. A more complex flow pattern is established in the bridge region, that is, in the clearance zone located in-between the rotors (Figure 5A). As visible in the magnification of the flow field of Figure 5B, a significant mass exchange occurs between the lobes of the mixing chamber: each rotor pumps the fluid in the bridge region where the flow is swept by the other rotor rotation. This is in agreement with the experimental observations obtained by flow field visualization studies.[4,5]

A recirculation pattern is also established in the small gap between the rotor tip and the chamber wall. As illustrated in the pressure contour plot of Figure 5C, in front of the rotor tip the pressure is consistently higher than the region behind it.[4,7] As a consequence, in the tip region the pressure flow opposes the drag flow, thus giving rise to the small recirculation visible in Figure 5D, which shows a magnification of the tip region.

The most crucial quantities in determining the breakup of the filler agglomerate are the shear rate, which provides a measure for the local intensity of the velocity gradients, and the mixing index, which instead provides a qualitative characterization of the flow field in terms of relative importance of the elongational and rotational component of the flow. The shear rate $\dot{\gamma}$ summarizes in one scalar quantity the velocity gradient components as follows:

$$\dot{\gamma} = 2\sqrt{II_{\mathbf{E}^\infty}} \tag{8}$$

where $II_{\mathbf{E}^\infty}$ is the second invariant of the rate-of-strain tensor $\mathbf{E}^\infty$.

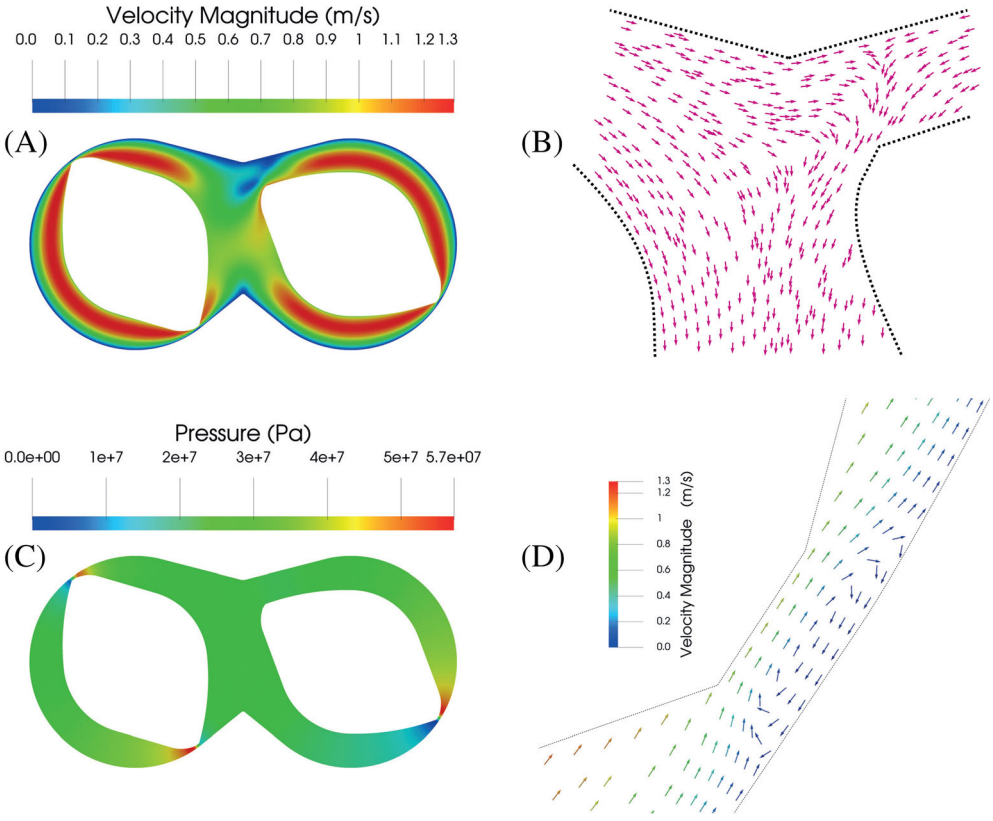

FIGURE 5 Instantaneous contour plots of: A, velocity magnitude; and C, static pressure. Magnification of: B, the velocity field in the bridge region; and D, at the chamber wall

Regarding the mixing index, here we make use of the Manas-Zloczower mixing index λ, which is defined as follows:

$$\lambda = \frac{\sqrt{II_{\mathbf{E}^\infty}}}{\sqrt{II_{\mathbf{E}^\infty}} + \sqrt{II_{\mathbf{\Omega}^\infty}}} \tag{9}$$

where $II_{\mathbf{\Omega}^\infty}$ is the second invariant of the vorticity tensor $\mathbf{\Omega}^\infty = 0.5(\nabla \mathbf{u}^\infty - \nabla \mathbf{u}^{\infty,T})$. The mixing index has a 0-1 range, with 0 indicating a rotational motion, and 0.5 and 1 indicating pure shear and pure elongational flow, respectively. The contours of these two derived quantities are reported in Figure 6A,B for the 1:1 speed ratio case. It is apparent that a wide scatter of the shear rate (Figure 6A) is present in the mixing equipment. The shear rate is relatively mild in the bridge region, whereas it takes on much larger values in the small gap between the rotor tip and the chamber wall, with a maximum value that is 20 times larger than the area-averaged shear in the entire equipment. In Figure 6B the distribution of the mixing index λ is also illustrated. It can be noted that the mixing index is 0.5 in most of the two lobe regions, whereas it reaches value close to 1 in the bridge region, indicating that the flow has a large elongational component in this region. However, for a complete characterization of the flow field, one should look at the joint probability distribution function of these two quantities; Figure 7 reports the joint probability distribution function of the shear rate and mixing index with their monovariate distribution, both weighted on the number of cells. The mixing index shows a single peak centered at pure shear conditions, whereas the shear rate distribution presents two distinguishable peaks occurring at $\dot{\gamma} \approx 7$ s^{-1} and $\dot{\gamma} \approx 30$ s^{-1}.

The area-weighted shear in the mixing chamber is reported as a function of time in Figure 8; it can be seen that for both speed ratios, $\langle \dot{\gamma} \rangle$ oscillates around 15.5 s^{-1} with a behaviour that proves that periodic flow conditions are established in the mixing equipment in both cases. The dashed vertical lines highlight the subdivision of the simulated time lapse in two subsequent periods.

In Table 3 the values of the average and maximum shear rate and mixing index are reported for the two different speed ratios investigated. The table also reports these quantities as sampled by the tracer particles. The numerical values of the quantities are rather similar, suggesting that the tracer particles sampled the flow field homogeneously. A discrepancy can only be noted in the average mixing index seen by the particles, which is rather larger than the mixing index averaged over the flow domain. This can be simply explained by considering the relatively large residence time of the tracers in the bridge region, where the largest mixing index values are observed.

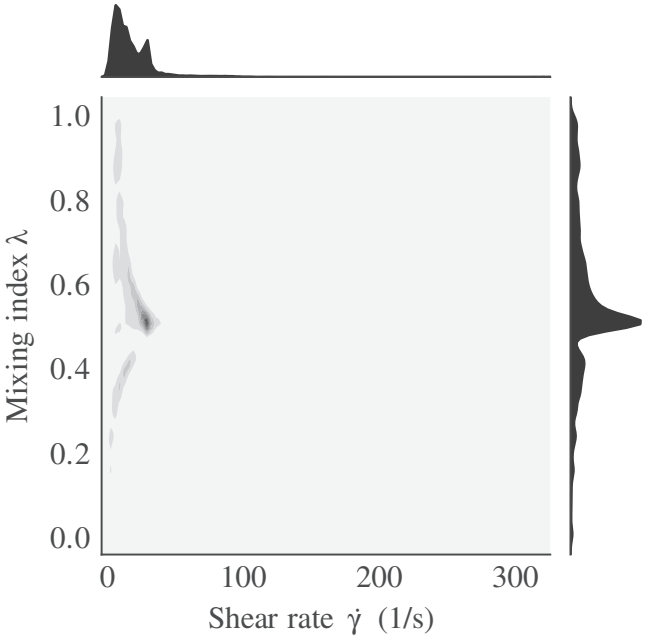

FIGURE 7 Joint probability distribution function of shear rate and mixing index

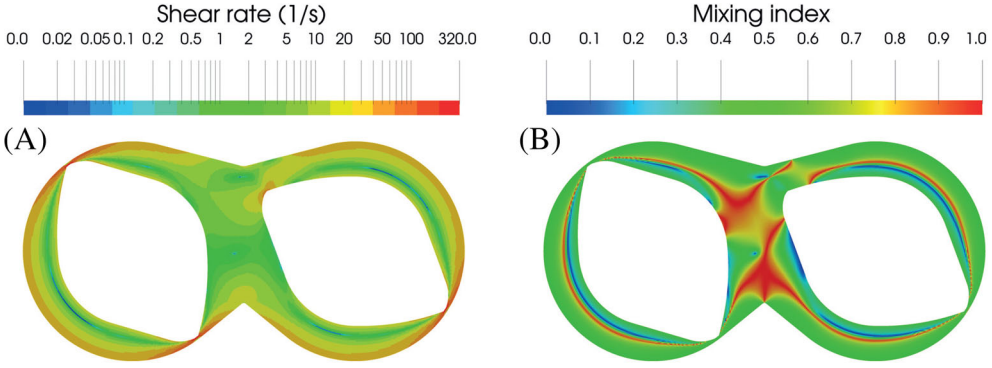

FIGURE 6 Instantaneous contour plots of: A, shear rate; and B, mixing index

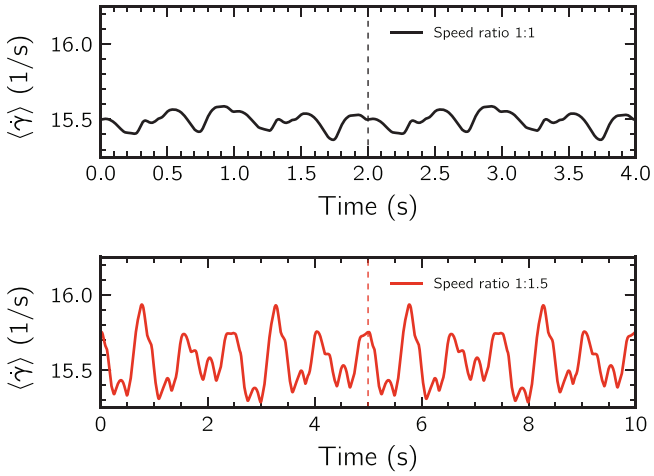

FIGURE 8 Area-weighted shear rate for two different speed ratios of the rotors (24 rpm:36 rpm) and (30 rpm:30 rpm). The dashed vertical lines subdivide the simulated time lapse in two periods

TABLE 3 Summary of the flow characteristics for the two investigated speed ratios

	1:1		1:1.5	
	Flow	**Tracers**	**Flow**	**Tracers**
$\langle\dot{\gamma}\rangle$ (s^{-1})	15.49	16.83	15.56	16.40
$\dot{\gamma}_{max}$ (s^{-1})	323.70	307.67	383.79	357.02
$\langle\lambda\rangle$	0.572	0.726	0.566	0.734

3.2 | Stress distribution in the agglomerates

The mechanical response of the agglomerates to the flow field was computed by running DEM simulations along the trajectories provided by the interpolation of the flow field obtained by the CFD simulations.

Figure 9 reports an instantaneous distribution of the hydrodynamic forces acting on each monomer as computed by the DEM; in the small inset, the local flow field experienced by the agglomerate is also represented. It can be noted that large hydrodynamic forces act on the most external monomers, whereas the inner monomers, because of the screening effects, experience on average lower forces. This force distribution leads to the normal stress distribution shown in Figure 10. In the figure, a ball and stick representation of the agglomerate has been used, where the shade intensity of the sticks provides a measure of the intensity of the tensile force N. It can be seen that the highest values of tensile stress arises in the most internal part of the agglomerate, quite far from the most loaded particles. This, as observed by previous researchers,[32] is the consequence of the low density structure of the agglomerate, which is made by contacting monomers arranged in such a way as to generate a filamentous structure along which the external load is propagated and accumulated.

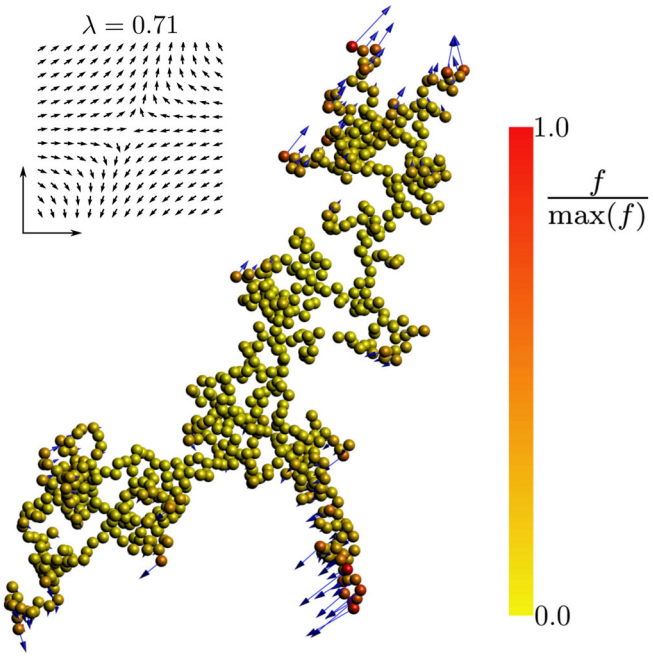

FIGURE 9 Distribution of the hydrodynamic force in an agglomerate made by 768 monomers. The shade intensity indicates the magnitude of the force. The direction of the force is shown for the monomers subject to the largest loads

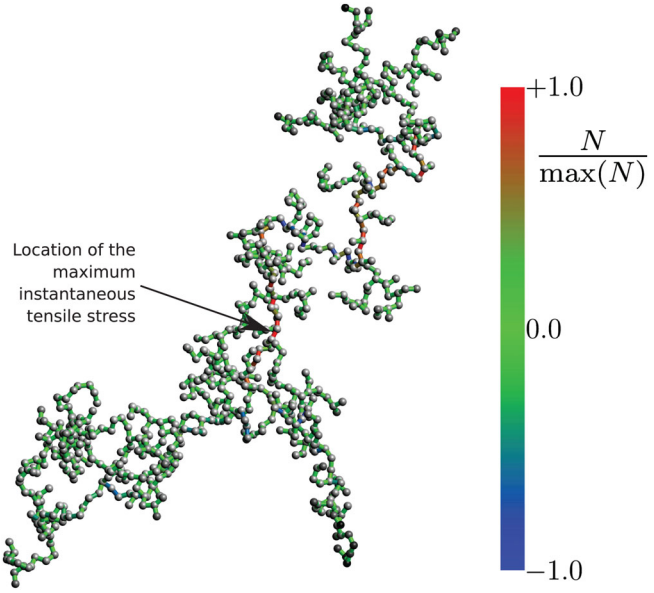

FIGURE 10 Normal force distribution via a ball and stick representation of the agglomerate structure. The highest tensile forces are observed in the most inner part of the agglomerate

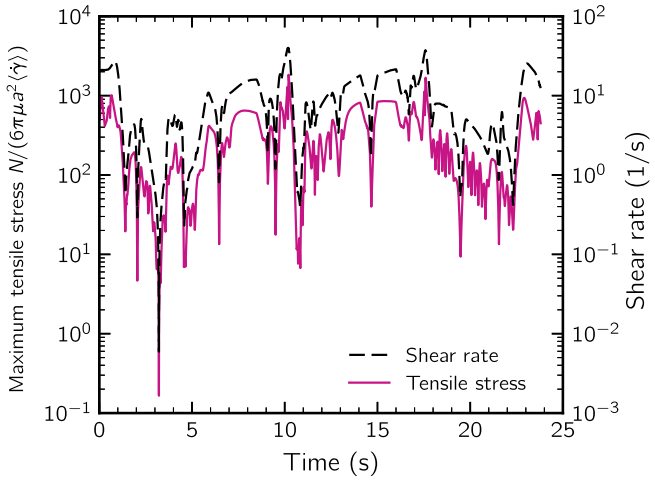

FIGURE 11 Shear rate signal experienced by an agglomerate (black dashed curve) and intensity of the maximum tensile stress inside the agglomerate (solid purple curve)

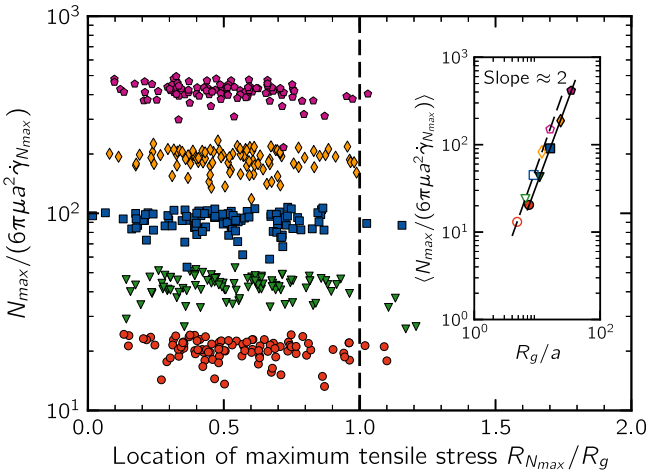

FIGURE 12 Scatter plot of the maximum instantaneous tensile stress and distance of the inter-monomer contact from the centre of mass of the agglomerate. In the inset, the scaling between the average tensile stress and the gyration radius of the agglomerate is shown. Empty symbols refer to a population with $d_f = 2.3$

Figure 11 reports the shear rate signal experienced by a 768-monomer agglomerate and the maximum induced tensile stress detected inside the structure. It is worth noting there is no time lag between the two signals, which present rather similar behaviours. This is due to two different reasons: the aggregates are considered perfectly rigid, and hence the transmission of the stress from the flow field to the agglomerate structure occurs instantaneously. Furthermore, since the agglomerate is quite large, and made by a large number of bonds, the presence of at least one bond oriented according to the direction of the maximum stress can be expected at any agglomerate orientation.

Figure 12 shows the maximum tensile stress N_{max} experienced by the agglomerates as a function of the distance of the inter-monomer contact from the centre of mass of the agglomerate. The data were obtained by simulating the mechanical response of 100 different agglomerates per class, each moving along a different trajectory over a total time lapse equal to 20 seconds. Each symbol in the plot represents the maximum tensile stress experienced by the agglomerate along its trajectory. It is apparent that, independently of the size, the maximum tensile stress is detected in the large majority of cases in the most internal part of the agglomerate, within one radius of gyration from the centre of mass, as highlighted by the dashed vertical line in the plot. Clearly, this feature is a consequence of the accumulation of stress along the filaments of the structure, as discussed before. Furthermore, it can be inferred from the plot that the expected dominant mechanism of breakup should be the fragmentation in two almost equally-sized daughter agglomerates, rather than the detachment of small chunks from the surface of the agglomerate in an erosion mechanism of size reduction. Finally, the plot further shows that as the size of the agglomerate increases, larger tensile stresses are observed inside the structure. A scaling between the average tensile stress and the size of the agglomerate was found, as shown in the inset. The proportionality between N and R_g^2can be explained by considering that the tensile stresses originate from the accumulation of hydrodynamic forces that are proportional in a first approximation to the radial coordinate of the monomer, along chains of length approximately equal to R_g.[32,33]

The analysis was also performed for denser, but still isostatic, agglomerates (with $d_f = 2.3$). The behaviour of this population has the same features of that with $d_f = 1.8$, both in terms of stress distribution and scaling law between size and internal normal stress (empty symbols in the inset of Figure 12). This suggests that as long as the agglomerates have an isostatic structure, the propagation of stresses from the exterior of the agglomerate towards the internal core should be expected.

3.3 | Breakup dynamics

To investigate the breakup dynamics of our agglomerates, we applied first-passage-time statistics on the tensile stress time series provided by the DEM simulations; we measured the distribution of the time τ_{brk} necessary for observing the first occurrence of a tensile stress strong enough to cause the failure of a bond and consequently the breakup of the agglomerate.[35,40] Considering an

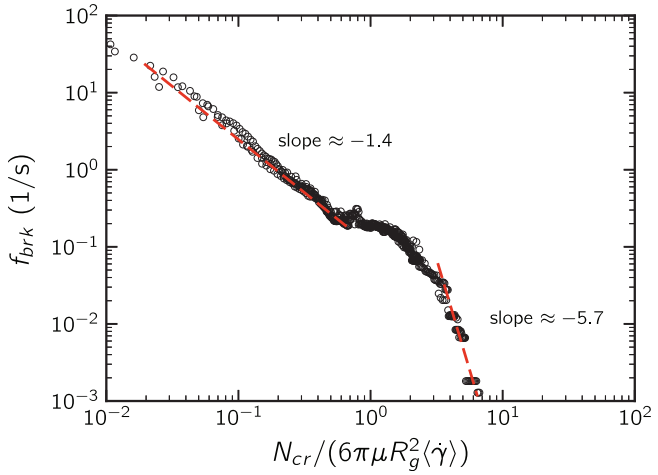

FIGURE 13 Breakup frequency as a function of the critical stress necessary for the failure of a bond. Data were obtained by averaging the breakup time over 1000 normal stress time series obtained by discrete element method simulations

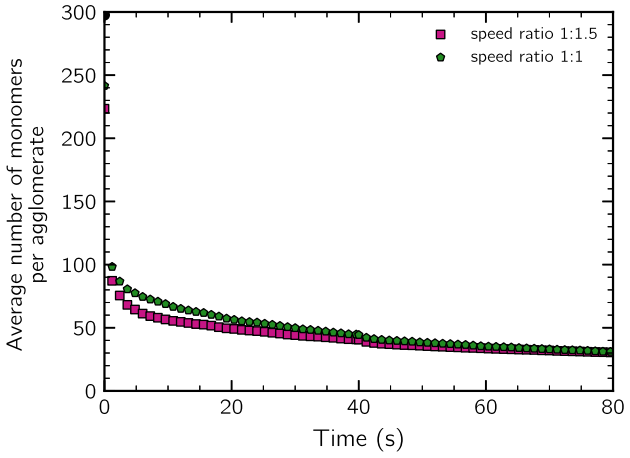

FIGURE 14 Population dynamics for $N_{cr}/(6\pi\mu a^2\langle\dot{\gamma}\rangle) = 130$ at two different speed ratio conditions: average agglomerate size as a function of time

agglomerate injected in the flow field at random space and time coordinates, its breakup time τ_{brk} is the time it needs to reach the condition $N > N_{cr}$ on any of its contacts for the first time (provided that at the injection time $N < N_{cr}$), where N_{cr} is the bond strength, that is, the maximum tensile force that a bond can sustain without breaking up. The breakup frequency was then computed as the inverse of the mean breakup time, obtained by averaging τ_{brk} over different injections, agglomerate realizations, and critical stresses. The results of the first-passage-time statistics for the case of a 1:1.5 speed ratio is shown in Figure 13. The data were obtained analyzing the normal stress time series of 1000 different agglomerates, each one moving along a distinct trajectory. We observed that the breakup frequencies of the different agglomerate classes collapse onto a single curve when normalizing the critical tensile stress N_{cr} with R_g^2. Hence, the plot of Figure 13 can be seen as a kinetic law giving the rate of fragmentation in the equipment as a function of agglomerate strength N_{cr}, size R_g and mean shear rate $\langle\dot{\gamma}\rangle$, when the system operates at a 1:1.5 speed ratio. Three distinct regions can be identified in the graph. For small values of N_{cr}/R_g^2 (ie, loose contacts and large agglomerates) the breakup frequency is large and scales as $N_{cr}^{-1.4}R_g^{2.8}$. For small agglomerates and strong contacts, the breakup frequency is lower and drops more rapidly as $N_{cr}^{-5.7}R_g^{10.4}$. A transition regime in which the breakup frequency remains almost constant was also observed for intermediate values of N_{cr}/R_g^2. However, it is worth pointing out that these breakup regimes and the scaling observed between the size and the internal resistance of the agglomerates have to be considered valid only for the flow investigated here and for the low-density agglomerate structure used.

We finally tracked the fate of a population of agglomerates composed of five classes, each of which is formed by 100 different agglomerates, for a prescribed value of N_{cr}. We released the different agglomerates at random positions inside the mixing chamber and we tracked each of them until the breakup condition $N > N_{cr}$ was reached. When this occurred, we detected the inter-monomer contact at which the condition was met and, based on this information, we produced the morphology of the two newly generated smaller agglomerates. Each fragment was tracked until the breakup condition was met again. This resulted in a cascade of breakup events, which produced, in the large majority of cases, two almost equally sized agglomerates.

Figure 14 reports the temporal trend of the population average size expressed in terms of number of constituent monomers for two different speed ratio conditions. From the plot, one can note that a drastic reduction of the average size occurs at the very beginning of the process for both cases. This is followed by a relative long phase in which the size reduction proceeds more gradually, until a constant average size is achieved. This is mainly due to the fact that the larger agglomerates breaks quite soon at the beginning of the process, as they experience larger internal stresses even if located in zone of relatively low shear forces. On the contrary the breakup of the smaller agglomerates is more sensitive to their orientation dynamics and to the fluid dynamics in the chamber; as they move in the mixing chamber carried by the flow, they experience a wide spectrum of shear forces, but it is only when the shear stresses are strong enough and the orientation is favourable that breakup occurs.

The slight difference in the initial trend for the two speed ratios is the consequence of the different flow

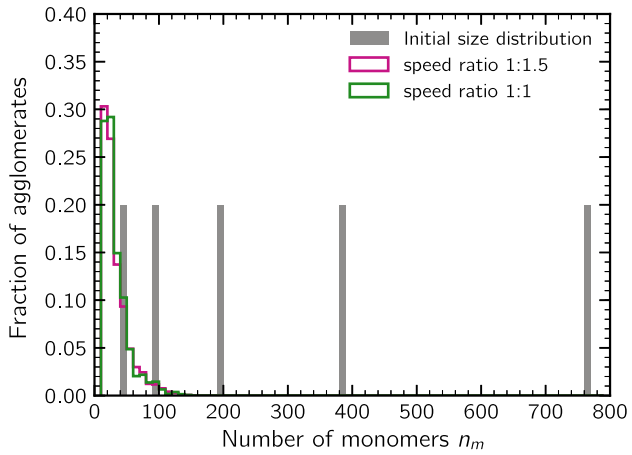

FIGURE 15 Population behaviour for $N_{cr}/(6\pi\mu a^2\langle\dot{\gamma}\rangle) = 130$ at two different speed ratio conditions: initial and final agglomerate size distribution

dynamics and different shear rate distribution in the mixing chamber. In the two cases, 1:1.5 (24 rpm:36 rpm) and 1:1 (30 rpm:30 rpm), the flow dynamics and the distribution of the shear rate are different; in the uneven speed ratio case there are zones close to the faster rotating rotor, in which the shear rate is larger compared to the even speed ratio case and where breakup is thus favoured. However, in the two cases, the same average shear rate establishes in the chamber. Therefore once particles have experienced the whole spectrum of the hydrodynamic stress, a similar stable average size is reached in the two cases; hence, for the adopted operative conditions the breakup dynamics is dictated primarily by the internal resistance of the agglomerates. This can also be inferred from the agglomerate size distribution sampled at $t = 80$ seconds, shown in Figure 15. For the same agglomerate strength the two populations show very similar final size distributions, both peaking at $n_m = 20$-30 and with a quite long tail extending up to $n_m = 160$.

4 | CONCLUSIONS

In this paper we presented a methodology to study the breakup of fractal agglomerates during a compounding operation. The method uses transient CFD simulations to evaluate the flow field in the mixing equipment and DEM simulations to study the mechanical response of the agglomerates to the viscous stress acting on them. Based on the negligible inertia of the agglomerates, we assumed during the CFD simulation that the agglomerates behave as point tracer particles, carried passively by the flow field. Conversely, in DEM simulations the typical disordered structure of the agglomerate was explicitly taken into account. By using Stokesian dynamics we were able to evaluate the hydrodynamic force acting on each monomer composing an agglomerate and to evaluate, by simple force balances, the normal force acting at each inter-monomer contact, to finally ascertain the occurrence of breakup.

We characterized the flow patterns for two different speed ratio conditions, showing the presence of a small recirculation zone in the gap between the rotor tip and the chamber wall and the mechanism of mass exchange between the lobes of the mixing chamber. The flow patterns were further characterized in terms of shear rate and mixing index, revealing the presence of a small thin region between the rotor tip and the chamber wall, where the shear rate takes on values substantially larger than the area-weighted ones; furthermore, we showed the presence of a region in-between the rotors where the elongational component of the flow prevails.

The DEM simulations allowed us to study the phenomena occurring at the agglomerate scale. We first analyzed the stress distribution inside the agglomerate structures as a response to the viscous stress exerted by the flow. Results showed that, at least for the rigid and isostatic agglomerates used here, a significant propagation and accumulation of stress takes place along the filamentous structure of the agglomerates. This suggests that for low density agglomerates the dominant mechanism of breakup is the fragmentation in two almost equally sized daughter agglomerates. The breakup rates of the agglomerates were evaluated by applying first-time-passage statistics on the tensile time series provided by the DEM simulations at varying agglomerate strengths; we observed the presence of two limiting breakup regimes for which a power-law correlation between the breakup frequency and the critical stress holds. Finally, we followed the evolution of the agglomerate size distribution by explicitly taking into account the location of bond failure and the resulting morphologies of the fragments. A stable final size distribution of the agglomerate was reached and seen to be dependent primarily upon the agglomerate strength.

The method has been applied here on a model set of operative conditions, but it can be tuned, for instance, to address the study of the breakup in non-Newtonian media or for differently structured agglomerates, for example, characterized by more compact structures or with a number of sintered, unbreakable contacts.

ACKNOWLEDGEMENTS

The work presented here has been developed in the context of the Virtual Material Marketplace project (www.vimmp.eu). The project leading to this application has received funding from the European Union's Horizon

2020 research and innovation programme under grant agreement No 760907.

NOMENCLATURE

Roman letters

a	monomer radius (m)
d_f	fractal dimension
d_{tip}	rotor tip radius (m)
$\mathbf{E}$	strain rate tensor (s^{-1})
$\mathbf{F}$	force (N)
k_f	fractal pre-factor
n_m	number of monomers
$\mathbf{N}$	tensile force (N)
N_t	number of tracer particles
p	pressure (Pa)
R_g	gyration radius (m)
$\mathbf{S}$	stresslet (N · m)
t	time (s)
$\mathbf{T}$	torque (N · m)
$\mathbf{u}$	velocity (m · s^{-1})
$\mathbf{x}$	position vector (m)

Greek letters

$\dot{\gamma}$	shear rate intensity (s^{-1})
Δt	time step length (s)
$\dot{\theta}$	rotor angular velocity (rad · s^{-1})
λ	mixing index
μ	liquid viscosity (Pa · s)
ρ	density (kg · m^{-3})
$\boldsymbol{\sigma}$	stress tensor (Pa)
τ_{brk}	breakup time lag (s)
$\boldsymbol{\omega}$	angular velocity (rad · s^{-1})
$\boldsymbol{\Omega}$	vorticity tensor (s^{-1})

Subscripts

cm	agglomerate centre of mass
cr	critical
m, n	monomer indexes
p	tracer particle

Superscripts

c	contact
∞	undisturbed flow field

ORCID

Graziano Frungieri https://orcid.org/0000-0001-8452-5071
Gianluca Boccardo https://orcid.org/0000-0003-1264-8237
Antonio Buffo https://orcid.org/0000-0002-4152-0593
Daniele Marchisio https://orcid.org/0000-0002-9104-0571
Marco Vanni https://orcid.org/0000-0001-7039-7259

REFERENCES

[1] I. Manas-Zloczower, Z. Tadmor, *Mixing and Compounding of Polymers - Theory and Practice*, Carl Hanser Verlag, Munich, Germany **1994**.
[2] A. Limper, *Mixing of Rubber Compounds*, Carl Hanser Verlag, Munich, Germany **2012**.
[3] B. Alsteens, *PhD Thesis*, Université Catholique de Louvain, Louvain, Belgium **2005**.
[4] P. K. Freakley, W. Y. W. Idris, *Rubber Chem. Technol.* **1979**, *52*, 134.
[5] P. K. Freakley, S. R. Patel, *Polym. Eng. Sci.* **1987**, *27*, 1358.
[6] K. Min, J. L. White, *Rubber Chem. Technol.* **1987**, *60*, 361.
[7] J.-J. Cheng, I. Manas-Zloczower, *Polym. Eng. Sci.* **1989**, *29*, 1059.
[8] H.-H. Yang, I. Manas-Zloczower, *Int. Polym. Process.* **1992**, *7*, 195.
[9] S. A. Salahudeen, R. H. Elleithy, O. AlOthman, S. M. AlZahrani, *Chem. Eng. Sci.* **2011**, *66*, 2502.
[10] J. Liu, F. Li, L. Zhang, H. Yang, *Rubber Chem. Technol.* **1987**, *132*, 42496.
[11] P. Dhakal, S. R. Das, H. Poudyal, A. J. Chandy, *J. Appl. Polym. Sci.* **2017**, *134*, 44250.
[12] R. K. Connelly, J. L. Kokini, *Adv. Polym. Technol.* **2006**, *125*, 182.
[13] R. K. Connelly, J. L. Kokini, *AIChE J.* **2006**, *52*, 3383.
[14] I. Manas-Zloczower, A. Nir, Z. Tadmor, *Rubber Chem. Technol.* **1982**, *55*, 1250.
[15] P. M. Adler, P. M. Mills, *J. Rheol.* **1979**, *23*, 25.
[16] R. C. Sonntag, W. B. Russel, *J. Colloid Interface Sci.* **1987**, *115*, 378.
[17] A. Nir, A. Acrivos, *J. Fluid Mech.* **1973**, *59*, 209.
[18] S. W. Horwatt, D. L. Feke, I. Manas-Zloczower, *Powder Technol.* **1992**, *72*, 113.
[19] P. A. Cundall, O. D. L. Strack, *Geotechnique* **1979**, *29*, 47.
[20] V. Becker, H. Briesen, *Phys. Rev. E* **2008**, *78*, 061404.
[21] V. Becker, H. Briesen, *J. Colloid Interface Sci.* **2009**, *339*, 362.
[22] L. Sanchez Fellay, C. Twist, M. Vanni, *Acta Mech.* **2013**, *224*, 2225.
[23] K. Higashitani, K. Iimura, H. Sanda, *Chem. Eng. Sci.* **2001**, *56*, 2927.
[24] M. Fanelli, D. L. Feke, I. Manas-Zloczower, *Chem. Eng. Sci.* **2006**, *61*, 473.
[25] A. Gastaldi, M. Vanni, *J. Colloid Interface Sci.* **2011**, *357*, 18.
[26] L. Durlofsky, J. F. Brady, G. Bossis, *J. Fluid Mech.* **1987**, *180*, 21.
[27] J. F. Brady, G. Bossis, *Annu. Rev. Fluid Mech.* **1988**, *20*, 111.
[28] R. Seto, R. Botet, H. Briesen, *Phys. Rev. E* **2011**, *84*, 041405.
[29] S. Harada, R. Tanaka, H. Nogami, M. Sawada, *J. Colloid Interface Sci.* **2006**, *301*, 123.
[30] G. Frungieri, M. Vanni, *Can. J. Chem. Eng.* **2017**, *95*, 1768.
[31] R. Seto, R. Botet, G. Auernhammer, H. Briesen, *Eur. Phys. J. E: Soft Matter Biol. Phys.* **2012**, *35*, 128.
[32] M. Vanni, A. Gastaldi, *Langmuir* **2011**, *27*, 12822.
[33] M. Vanni, *Comput. Phys. Commun.* **2015**, *192*, 70.

[34] Y. M. Harshe, M. Lattuada, *J. Phys. Chem. B* **2016**, *120*, 7244.
[35] J. De Bona, A. S. Lanotte, M. Vanni, *J. Fluid Mech.* **2014**, *755*, 365.
[36] M. Horsch, C. Niethammer, G. Boccardo, P. Carbone, S. Chiacchera, M. Chiricotto, J. D. Elliott, V. Lobaskin, P. Neumann, P. Schiffels, M. Seaton, I. Todorov, J. Vrabec, W. Cavalcanti, *J. Chem. Eng. Data* **2020**, *65*, 1313.
[37] W. I. Thacker, J. Zhang, L. T. Watson, J. B. Birch, M. A. Iyer, M. W. Berry, *ACM Trans. Math. Software* **2010**, *37*, 34.
[38] R. Thouy, R. Jullien, *J. Phys. A: Math. Gen.* **1994**, *27*, 2953.
[39] A. Filippov, M. Zurita, D. Rosner, *J. Colloid Interface Sci.* **2000**, *229*, 261.
[40] M. U. Bäbler, L. Biferale, A. S. Lanotte, *Phys. Rev. E* **2012**, *85*, 025301.

How to cite this article: Frungieri G, Boccardo G, Buffo A, Marchisio D, Karimi-Varzaneh HA, Vanni M. A CFD-DEM approach to study the breakup of fractal agglomerates in an internal mixer. *Can J Chem Eng*. 2020;98: 1880–1892. https://doi.org/10.1002/cjce.23773